First-principles study of hydrogen storage in Ti-Fe-Hf-Ni alloys

Ellen Leib,* Tasneem Mazhar,† Olivier Nauwelaers,‡ and Tomas Verbist§

(Dated: December 6, 2025)

We present a first-principles study of the structural stability and hydrogen incorporation behavior of Ti–Fe, Ti–Ni, and Hf–Fe intermetallic compounds using density functional theory. An equation-of-state analysis of TiFe yields its equilibrium lattice constant and bulk modulus. Formation energies computed for multiple structural prototypes confirm that all compounds considered are thermodynamically stable at 0 K, with cubic Laves phases showing the strongest driving forces for formation. Hydrogen absorption was examined by inserting H at interstitial sites and relaxing the structures. In all studied alloys, H migrates toward specific symmetric Wyckoff positions, with TiFe exhibiting the most favorable incorporation energies and the weakest dependence on hydrogen content. These results provide insight into hydrogen uptake in Ti-based storage alloys and shows ways for tuning absorption energetics.

Keywords: hydrogen storage, density functional theory, TiFe, TiNi, HfFe

I. INTRODUCTION

Hydrogen as an energy carrier is considered essential for moving towards clean energy and replacing fossil fuels, but a safe, low-cost and efficient way of storage is currently lacking. Physical hydrogen storage methods, like compressed gas and liquid hydrogen, present challenges as they require highly energy-intensive processes for compression or cryogenic cooling, which introduce energy and safety constraints. Material-based storage methods, like using metal hydrides, offer a more compact and inherently safer alternative to physical storage [1, 2].

Among these options, TiFe is considered one of the most optimal candidates because of its high volumetric storage capacity (105 kg H_2/m^3) and low cost. In addition, TiFe can reversibly store and release hydrogen near room temperature and atmospheric pressure, which makes it attractive for stationary storage applications [3]. However, the alloy is difficult to activate as the surface becomes oxidized after exposure to air. Additionally, the first hydrogenation typically requires high pressures and temperatures above 400 °C. To address this problem, research is conducted to examine how alloying with substitutional elements such as Ni or Hf could lead to lower activation temperatures and how they influence the phase stability and hydrogen absorption [4].

Computational methods can support these efforts by providing an estimation for material properties and helping explore the fundamental mechanisms of hydrogen storage behavior in these alloys. In this project, we use density functional theory [DFT] to analyze the stability of different crystal structures, compare alloy formation energies and evaluate the energy cost of introducing hydrogen into different crystal lattices. The objective of our research is to identify which alloy compositions and interstitial sites are the most favorable for hydrogen storage.

II. METHODOLOGY

All calculations were performed using Quantum ESPRESSO [5, 6] with PBE pseudo-potentials. The standard solid-state pseudopotentials library [SSSP PBE Efficiency v1.3.0] [7] was used for all pseudopotentials.

A. Convergence testing on TiFe

Convergence testing is a crucial part of DFT calculations as the results of our calculations can be influenced by parameters such as `ecutwfc`, `ecutrho` and `k_points`, which represent cutoff values and for which the appropriate values are not known a priori. The goal of convergence testing is to determine the minimal values for which the computed observables change negligibly, ensuring that the results reflect physical behavior rather than random noise. In this step a TiFe crystal, as shown in Figure 4, is used. The `k_mesh` is optimized first, while `ecutwfc` and `ecutrho` are initially set to the default values from the Fe pseudopotential files. The computed hydrostatic pressure is used as the metric by which convergence is judged, since this property has the tendency to be heavily influenced by the aforementioned parameters. Next, the `ecutwfc` value is optimized while keeping `ecutrho` fixed as a constant multiple, after which the multiplication factor is adjusted to determine the optimal `ecutrho`.

B. E(V) curve for TiFe

We first characterized some properties of the TiFe $pm\bar{3}m$ crystal. The unit cell was uniformly scaled to generate 20 different volumes between 71% and 131% of its initial volume, and the total energy was computed for each case. This energy-volume data was fitted to the third-order Birch–Murnaghan isothermal equation of state, as shown in equation (B1). The equilibrium volume and bulk modulus were obtained from this fit.

Following this, a full geometry optimization of the TiFe crystal was performed. The optimized volume from this calculation was compared with the equilibrium value we derived from the EOS fit. Additionally, the volume change following the application of 10 GPa of external pressure was calculated. This was obtained by expressing the EOS (B1) in terms of volume as a function of pressure.

C. Formation energy for Ti-Fe, Hf-Fe and Ti-Ni crystals

Each intermetallic phase studied (TiFe, $TiFe_2$ (hexagonal and cubic), HfFe, $HfFe_2$ (hexagonal and cubic), TiNi, and $TiNi_2$ (hexagonal and cubic)) underwent a complete geometry optimization. This procedure (*VC-Relax*), relaxes both lattice parameters and internal atomic coordinates.

To ensure thermodynamic consistency, identical convergence thresholds for forces and stress were applied to all structures. After convergence, the total energies E_{tot}, equilibrium volumes, and magnetic moments were extracted from the final relaxed

---

* University of Tartu; ellen.leib@ut.ee

† North South University; tasneem.mazhar.252@northsouth.edu

‡ Universiteit Antwerpen; olivier.nauwelaers@student.uantwerpen.be

§ Universiteit Antwerpen; tomas.verbist@student.uantwerpen.be

configurations. The relaxed structural data from these calculations are summarized in Table II.

The formation energy per formula unit [fu] of each intermetallic compound A_xB_y was computed using the formula

$$\Delta E_{\mathrm{f}} = E_{\mathrm{tot}}(A_xB_y) - x\,E_{\mathrm{tot}}(A) - y\,E_{\mathrm{tot}}(B), \tag{1}$$

where $E_{\mathrm{tot}}(A_xB_y)$ is the total energy of the fully relaxed intermetallic structure normalized to a single formula unit, and $E_{\mathrm{tot}}(A)$ and $E_{\mathrm{tot}}(B)$ are the energies per atom of the relaxed elemental phases. Energies were converted from Rydberg to electronvolts and formation energies are reported per formula unit as well as per atom for easier comparison across compounds with different stoichiometries.

A negative ΔE_{f} indicates thermodynamic stability at zero Kelvin relative to decomposition into the elemental solid phases. Comparison of ΔE_{f} values across all phases in a binary system identifies the compounds expected to appear on the convex hull and thus be experimentally realizable.

D. Hydrogen at high symmetry sites in TiFe

Hydrogen incorporation in TiFe was investigated using a series of DFT calculations where H atoms were introduced into high symmetry interstitial positions of the TiFe unit cell. All simulations employed the converged plane-wave and k-point settings established in the previous steps. The convergence settings were verified again for the hydrogen containing TiFe structures.

TiFe crystallizes in the cubic space group Pm$\bar{3}$m, where Ti occupies the 1a Wyckoff site at $(0, 0, 0)$ and Fe occupies the 1b site at $(\frac{1}{2}, \frac{1}{2}, \frac{1}{2})$. Hydrogen atoms were inserted into representative high-symmetry interstitial Wyckoff positions permitted by this space group:

- 3d sites: $(0, \frac{1}{2}, \frac{1}{2})$, $(\frac{1}{2}, 0, \frac{1}{2})$, $(\frac{1}{2}, \frac{1}{2}, 0)$,
- 3c sites: $(\frac{1}{2}, 0, 0)$, $(0, \frac{1}{2}, 0)$, $(0, 0, \frac{1}{2})$,
- 8g site: $(\frac{1}{4}, \frac{1}{4}, \frac{1}{4})$.

Configurations containing one, two, or three hydrogen atoms were constructed by occupying these sites in accordance with the crystal symmetry. Both lattice parameters and atomic coordinates were relaxed in all TiFe–H structures. For each configuration, the hydrogen incorporation energy per atom was calculated using

$$E_{\mathrm{H}} = \frac{E(\mathrm{TiFe} + n\mathrm{H}) - E(\mathrm{TiFe})}{n},$$

where n is the number of hydrogen atoms inserted into the unit cell. This quantity is directly analogous to a hydrogen formation energy and quantifies the energetic favourability of hydrogen uptake. No significant changes were necessary, and the previously converged cutoff and k-mesh values were used for all TiFeH optimisations.

E. Optimal Hydrogen storage positions in TiFe, HfFe and TiNi crystals

We evaluated both the energy cost of hydrogen incorporation in fully relaxed TiFe, HfFe and TiNi crystals and the preferred positions of the added hydrogen into the unit cell through a series of DFT calculations. A 12x12x12 grid search of each of the mentioned cells was performed where a singular hydrogen atom was placed at a site within the unit cell. At each grid point a DFT *relax* calculation was carried out, keeping the unit cell parameters constant, while the atomic positions were allowed to relax. All simulations employed the previously converged plane-wave and k-point settings.

The most energetically preferred interstitial positions by the hydrogen atoms in the grid search were further investigated by constructing configurations containing one, two, or three hydrogen atoms at these sites. These configurations were then fully optimized using *vc-relax* DFT calculations where both lattice parameters and atomic coordinates were allowed to relax in all structures.

III. RESULTS

A. Convergence testing on TiFe

The converged data are summarized in Figure 5. The final parameters found are: `k_mesh:11×11×11`, `ecutwfc: 140` and `ecutrho: 1260`. These values are applied in all subsequent calculations, even when different unit cells are used. Since `k_mesh` is found to strongly impact the computation time, its value is scaled based on the dimensions of the unit cells, according to formula (A1). This ensures that the density of k-points in reciprocal space remains approximately constant when the real-space lattice dimensions change.

B. $E(V)$ curve for TiFe

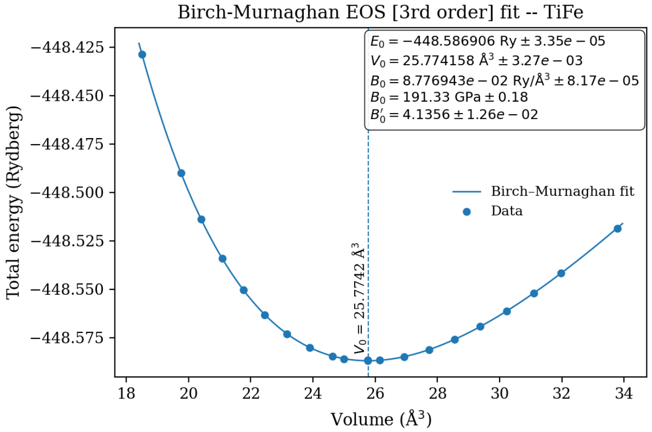

FIG. 1: Third-order Birch–Murnaghan equation-of-state fit to the TiFe $E(V)$ data. Error bars reflect deviations of the DFT points from the fitted curve.

The data used for the $E(V)$-calculations for TiFe $pm\bar{3}m$ are shown with the EOS fit in Figure 1. Table I lists the the equilibrium volume and bulk modulus of the TiFe crystal that we determined using the EOS-fit. The values reported in Table I contain two conceptually different uncertainties. The uncertainties that arise from the Birch–Murnaghan fit covariance matrix reflect the *fit precision* to our computed $E(V)$ points and do not capture the typical spread between PBE predictions and experiment (i.e. the accuracy). To provide an uncertainty that is meaningful for comparison with experiments, we follow [8] who recommend applying a regression correction followed by an intrinsic residual error bar (SER) that quantifies the typical PBE scatter versus the experiment. Since the effect of zero-point vibrations is only very minor, it was neglected for these calculations.

In [9], it can be seen that the Voight, Reuss and Voigt-Reuss-Hill bulk modulus are all reported to be 199 GPa which is in almost perfect agreement with out corrected value of 200.7 GPa, and well within the expected PBE accuracy range. The equilibrium volume for the unit cell was determined in two ways: via the EOS fit, as well as by performing a VC-relax calculation, yielding a result of respectively 25.7741 Å^3 (uncorrected) and 25.7980 Å^3. These values agree closely and provide an internal consistency check showing one interesting aspect of performing DFT calculations: the possibility to calculate one property via different ways and thus perform internal validation.

TABLE I: Equilibrium volume and bulk modulus of TiFe obtained from the third-order Birch–Murnaghan EOS fit. Errors for the [EOS fit] refer to the 1σ uncertainty from the fit covariance matrix. The regression corrected [RC] and final uncertainty follow the recommendation of [8] and use the PBE systematic correction and standard error of regression [SER] making comparison with empirical results possible.

Property	**Value**
Eq. Volume [EOS fit]	(25.7741 ± 0.0033) Å^3
Eq. Volume (RC)	24.8462 Å^3
Eq. Volume (SER)	(24.846 ± 1.100) Å^3
Bulk modulus [EOS fit]	(191.33 ± 0.18) GPa
Bulk modulus [RC]	200.705 GPa
Bulk modulus [SER]	(200.7 ± 15.0) GPa
Eq. Volume [relaxation]	25.7980 Å^3

Finally, we estimated how much the volume would change if one were to apply an external pressure of 10 GPa. Using the fitted third-order Birch–Murnaghan EOS (V_0=25.774 Å^3, B_0 =191.3 GPa, $B_0' = 4.14$), compression to 10 GPa reduces the equilibrium volume to 24.581 Å^3, i.e. a volume contraction of 4.63%. A first-order estimate ($\Delta V/V \approx -P/B_0$) would give a reduction of $\sim$ 5.23%, so finite-strain corrections (captured by the BM equation) reduce the predicted contraction slightly.

C. Formation energy for Ti-Fe, Hf-Fe and Ti-Ni crystals

The formation energies for the Ti–Fe system are presented in Table III. All three investigated compounds (i.e. TiFe, and the two $TiFe_2$ polymorphs) exhibit negative formation energies, consistent with thermodynamic stability at zero temperature. Among them, the cubic Laves phase ($Fd\bar{3}m$) shows the most negative formation energy (−0.301 eV/atom), followed closely by the hexagonal C14 variant. TiFe, with the B2 ($Pm\bar{3}m$) structure, is also quite stable with a formation energy of approximately −0.429 eV/atom. This hierarchy is in line with the experimental Ti–Fe phase diagram, where both TiFe and $TiFe_2$ are recognized stable phases [10].

Table IV shows the formation energies for the Hf–Fe system. All three investigated compounds again show negative formation energies, indicating that they are stable against elemental decomposition. Compared to $TiFe_2$, the Hf_2-containing polymorphic compounds exhibit even more negative formation energies, with the cubic $HfFe_2$ phase showing the largest driving force for stability at −0.357 eV/atom, closely mirroring the energetic trends in the $TiFe_2$ series. HfFe is also stable at approximately −0.332 eV/atom.

Experimentally, the Hf–Fe phase diagram contains stable cubic $HfFe_2$ but no HfFe phases [11]. Again the theoretical stability ordering is fully consistent with observed compounds. It is known that the difference in the structural energies of the laves polytypes are small due to the close relation between their crystal structures, i.e. there are very similar nearest-neighbour geometries [11]. We believe that the larger stability of Hf-based intermetallics relative to the Ti-based ones might come from the stronger chemical bonding of the heavier group-IV metal with Fe due to their more delocalized 5*d* electrons.

The relaxed structures and formation energies for the Ti–Ni system are reported in Table V. All three intermetallics exhibit negative formation energies, confirming their computational thermodynamic stability. As in the Fe-based binaries, the cubic Laves phase has the most negative formation energy and is thus predicted to be the thermodynamically preferred $TiNi_2$ variant. Experimentally, TiNi is a stable compound, however $TiNi_2$ does not seem to exist in Ti–Ni phase diagrams [12].

All investigated compounds have negative formation energies and are therefore predicted to be thermodynamically stable at $T = 0$ K. Also, the cubic Laves phases ($Fd\bar{3}m$) are systematically the most stable among the respective AB_2 compositions

D. Hydrogen at high symmetry sites in TiFe

The energies and volumes of the relaxed structures are reported in Table VI, in the rows labeled by TiFe. A comparison of our DFT results shows a preferred ordering of hydrogen sites in the TiFe unit cell. In decreasing energy per H atom, the configurations are:

$$\mathrm{TiFe\_0} > \mathrm{TiFe\_4} > \mathrm{TiFe\_2} > \mathrm{TiFe\_1} > \mathrm{TiFe\_3} > \mathrm{TiFe\_5}.$$

Naming conventions are reported in table VI. The differences in energy per H atom show that there are preferential hydrogen configurations. In practice, it would be expected that hydrogen will occupy the most energetically favorable sites during storage. The next subsection examines whether hydrogen placed randomly in the unit cell will migrate toward these symmetrical positions investigated here, across different cells.

An important note to make is that the calculated absolute values for the energies do not correspond to those found in literature. This is due to the zero-point correction, which has not been included in our current treatment. Zero-point energy (ZPE) arises from the quantum mechanical contribution of each vibrational mode and is especially important for light atoms such as hydrogen. ZPE corrections may reduce the reported energy gaps between configurations, and could in principle alter the ordering of the lowest-energy sites. In this work, the relative trends remain useful for identifying preferential H sites, however the reported absolute values cannot be compared to literature. For future calculations, we recommend evaluating the ZPE per H and reassessing the ordering for the smallest of the energy gaps.

E. Optimal Hydrogen storage positions at high symmetry sites in TiFe, HfFe and TiNi crystals

Figure 2 shows a composite image of how a hydrogen atom, initially placed at various points of a 12×12×12 grid within the TiFe unit cell, moves during DFT relaxation (an enlarged view is provided in Figure 6). Because each calculation involves only a single hydrogen atom at a time, the resulting trajectories represent the natural relaxation paths for singular H atoms in the unit cell. As shown in Figure 2, the hydrogen consistently migrates toward high-symmetry sites within the TiFe unit cell. A similar evolution can be seen in figures 7 and 8 for the HfFe and TiNi crystals respectively. In each case, when a single H atom is placed at various positions within the unit cell and the structure is allowed to relax, it moves towards these preferred high-symmetry sites (Wyckoff positions) [13]:

1. TiFe: 3c: $(0, 1/2, 1/2)$, 3d: $(0, 1/2, 1/2)$
2. HfFe: 6e: $(x, 0, 0)$, 3c: $(0, 1/2, 1/2)$, 3d: $(0, 1/2, 1/2)$
3. TiNi: 6e: $(x, 0, 0)$, 3c: $(0, 1/2, 1/2)$

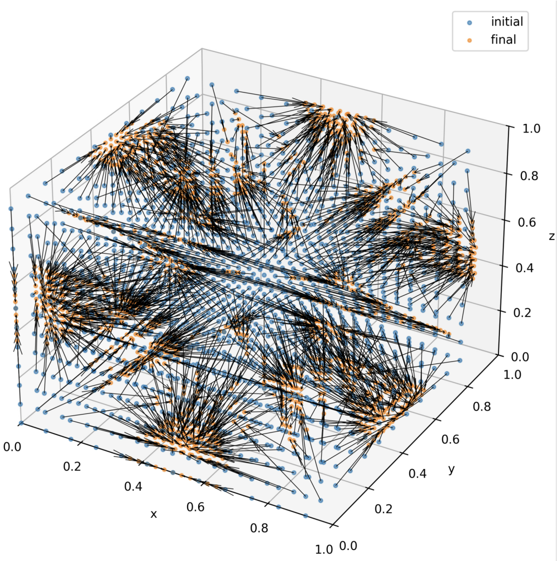

FIG. 2: Graphical representation of the displacement of hydrogen atoms in the TiFe unit cell during DFT relaxation. Arrows indicate the direction of atomic movements toward preferred high-symmetry Wyckoff positions (3c and 3d).

The final positions of Ti, Fe, Hf, Ni and H for each of the three crystals are shown in Figures 9, 10 and 11 as 2D projections of Figures 6, 7 and 8.

In TiFe, the Ti and Fe atoms move the least of all cells. Their final positions do not show any outliers and a compact, regular pattern is visible corresponding to an isotropic spherical spread. In HfFe there are many outliers and the atoms move more than they did in TiFe. Hf shows the same regular pattern as Fe in TiFe, but with a more pronounced spread. Hf however exhibits a different pattern compared to Ti in TiFe. It seems to form a central spot with arrow-like arms in the x, y and z directions forming a cross. It is possible that this pattern in also present in TiFe but not visible due to the smaller amount of movement of the atoms. TiNi shows the largest amount of movement, both Ti and Ni move in very specific, regular directions, exhibiting the same patterns as observed in HfFe, but more clearly visible with less deviation from this arrow-like pattern. The total movement within TiFe is the lowest, within TiNi it's the highest. The movement of the heavier elements in TiNi is especially pronounced, as one can see on the histograms in Figure 12.

Since we always used the fully relaxed crystal without hydrogen as a starting point, we wanted to exclude the possibility that the observed differences were due to the effect hydrogen would have on the volume. To exclude this possibility, calculations were ran with the volume changed to −5% and +5%. This didn't seem to impact the observed results. Since the symmetry is the same for all crystals, the difference in movement between the atoms can most likely be explained by the different electronic structure of the elements. To evaluate this, electron density difference plots were generated, but these were found difficult to directly link to the displacement of internal elements.

High-symmetry positions are further examined by placing varying numbers of hydrogen atoms in different configurations at these preferential sites within each crystal. Due to computational constraints, the list of tested configurations is necessarily non-exhaustive [14].

In total, a maximum of three hydrogen atoms are added, resulting in 138 possible configurations, from which $9_{\mathrm{HfFe}} + 5_{\mathrm{TiFe}} + 5_{\mathrm{TiNi}} = 19$ symmetrically-nonequivalent configurations are selected [15]. Table VI summarizes the results obtained after allowing both the atomic positions and cell parameters to relax, the resulting energies per hydrogen atom are shown in Figure 3.

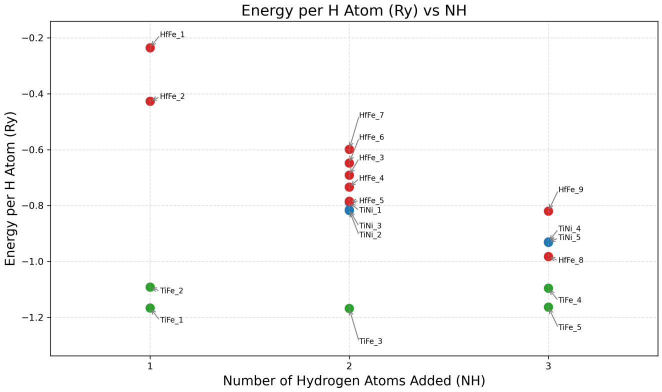

FIG. 3: A graphical representation of the energy per hydrogen atom for symmetrically selected interstitial configurations in TiFe (green), TiNi (blue), and HfFe (red) as a function of hydrogen loading (NH = 1–3).

TiFe consistently exhibits the lowest energies (−1.25 to −1.15 Ry per H), followed by TiNi (−0.95 to −0.85 Ry) and HfFe (−1.0 to −0.25 Ry), indicating TiFe as being the most favorable hydrogen-binding host.

It is also apparent that loading affects the systems differently: TiFe shows minimal energy variation with increasing N_{H}, this could indicate that each consecutive hydrogen atom added does not significantly affect the energy landscape for the following hydrogen atoms. TiNi shows a slight decrease in energy at higher hydrogen loadings. HfFe displays a strong loading dependence, with the widest energy spread among configurations at each H count. TiNi, by contrast, exhibits the smallest variation. These trends should be interpreted cautiously: the limited amount of data and non-converging configurations, summarized in Table VI, restrict the range of reliably tested structures and calls for further investigation.

IV. CONCLUSION

Our DFT study shows that all investigated intermetallics (TiFe, TiNi and HfFe families) are thermodynamically stable at T=0 K with the cubic Laves polymorphs consistently exhibiting the most negative formation energies. Hydrogen incorporation calculations identify TiFe as the most favorable host for H (lowest incorporation energies and weakest dependence on loading), while HfFe displays the largest sensitivity to hydrogen content and TiNi intermediate behaviour. Grid-search relaxations demonstrate that single H atoms migrate to crystal specific high-symmetry Wyckoff sites, also showing differences in the movements of the elements between the different crystals.

---

[1] H. Liu, J. Zhang, P. Sun, C. Zhou, Y. Liu, and Z. Z. Fang, An overview of TiFe alloys for hydrogen storage: Structure, processes, properties, and applications, Journal of Energy Storage **68**, 107772 (2023).

[2] S. O. Akpasi, I. M. Smarte Anekwe, E. K. Tetteh, U. O. Amune, S. I. Mustapha, and S. L. Kiambi, Hydrogen as a clean energy carrier: Advancements, challenges, and its role in a sustainable energy future, Clean Energy **9**, 52 (2025).

[3] E. M. Dematteis, N. Berti, F. Cuevas, M. Latroche, and M. Baricco, Substitutional effects in TiFe for hydrogen storage: a comprehensive review, Materials Advances **2**, 2524 (2021).

[4] K. Komkedera, J. Michalik, K. Sworst, *et al.*, Structure, microstructure and hyperfine interactions in Hf-and Ni-substituted TiFe alloy for hydrogen storage, Acta Physica Polonica A ISSN 1898-794X **146**, 215 (2024).

[5] P. Giannozzi, S. Baroni, N. Bonini, M. Calandra, R. Car, C. Cavazzoni, D. Ceresoli, G. L. Chiarotti, M. Cococcioni, I. Dabo, A. Dal Corso, S. de Gironcoli, S. Fabris, G. Fratesi, R. Gebauer, U. Gerstmann, C. Gougoussis, A. Kokalj, M. Lazzeri, L. Martin-Samos, N. Marzari, F. Mauri, R. Mazzarello, S. Paolini, A. Pasquarello, L. Paulatto, C. Sbraccia, S. Scandolo, G. Sclauzero, A. P. Seitsonen, A. Smogunov, P. Umari, and R. M. Wentzcovitch, QUANTUM ESPRESSO: a modular and open-source software project for quantum simulations of materials, Journal of Physics: Condensed Matter **21**, 395502 (19pp) (2009).

[6] P. Giannozzi, O. Andreussi, T. Brumme, O. Bunau, M. B. Nardelli, M. Calandra, R. Car, C. Cavazzoni, D. Ceresoli, M. Cococcioni, N. Colonna, I. Carnimeo, A. D. Corso, S. de Gironcoli, P. Delugas, R. A. D. Jr, A. Ferretti, A. Floris, G. Fratesi, G. Fugallo, R. Gebauer, U. Gerstmann, F. Giustino, T. Gorni, J. Jia, M. Kawamura, H.-Y. Ko, A. Kokalj, E. Küçükbenli, M. Lazzeri, M. Marsili, N. Marzari, F. Mauri, N. L. Nguyen, H.-V. Nguyen, A. O. de-la Roza, L. Paulatto, S. Poncé, D. Rocca, R. Sabatini, B. Santra, M. Schlipf, A. P. Seitsonen, A. Smogunov, I. Timrov, T. Thonhauser, P. Umari, N. Vast, X. Wu, and S. Baroni, Advanced capabilities for materials modelling with QUANTUM ESPRESSO, Journal of Physics: Condensed Matter **29**, 465901 (2017).

[7] G. Prandini, A. Marrazzo, I. E. Castelli, N. Mounet, and N. Marzari, Precision and efficiency in solid-state pseudopotential calculations, npj Computational Materials **4**, 72 (2018), http://materialscloud.org/sssp.

[8] K. Lejaeghere, V. Van Speybroeck, G. Van Oost, and S. Cottenier, Error Estimates for Solid-State Density-Functional Theory Predictions: An Overview by Means of the Ground-State Elemental Crystals, Critical Reviews in Solid State and Materials Sciences **39**, 1 (2014).

[9] Materials data on TiFe by Materials Project 10.17188/1204904 (2020).

[10] P. O'Kelly, A. Watson, G. Schmidt, M. Galetz, and A. J. Knowles, Ti-Fe Phase Evolution and Equilibria Toward beta-Ti Superalloys, Journal of Phase Equilibria and Diffusion **44**, 738 (2023).

[11] M. Idbenali, N. Selhaoui, L. Bouirden, and C. Servant, Thermodynamic assessment of the Fe–Hf binary system, Journal of Alloys and Compounds **456**, 151 (2008).

[12] D. Cascadan and C. Roberto Grandini, Structure, Microstructure, and Some Selected Mechanical Properties of Ti-Ni Alloys, in *Recent Advancements in the Metallurgical Engineering and Electrodeposition*, edited by U. Basheer Al-Naib, D. Vikraman, and K. Karuppasamy (IntechOpen, 2020).

[13] For other equivalent positions per Wyckoff position, we refer to the *International Tables for Crystallography*, specifically the Wyckoff positions of space group Pm$\overline{3}$m (No. 221).

[14] The three crystals combined admit 4669 possible configurations using the found positions, many of which are symmetrically equivalent. This shows the need to select only the most relevant cases.

[15] An additional seven configurations were tested, but these failed to converge within a reasonable time and are therefore omitted from the discussion.

Appendix A: Convergence testing

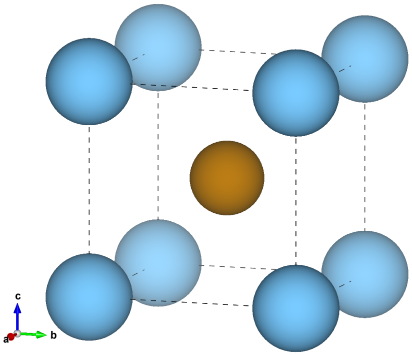

FIG. 4: Unit cell of TiFe used in the convergence testing. The structure corresponds to a primitive lattice (space group *P1*) with lattice parameters $a = b = c = 2.93868$ Å and $\alpha = \beta = \gamma = 90°$, giving a unit-cell volume of 25.377988 Å^3. The cell contains one titanium atom located at $(0, 0, 0)$ and one iron atom at $(0.5, 0.5, 0.5)$, each with full site occupancy.

$$N_i \;=\; \left\lceil N_i^{\mathrm{TiFe}}\,\frac{a_{\mathrm{TiFe}}}{a_i}\right\rceil \tag{A1}$$

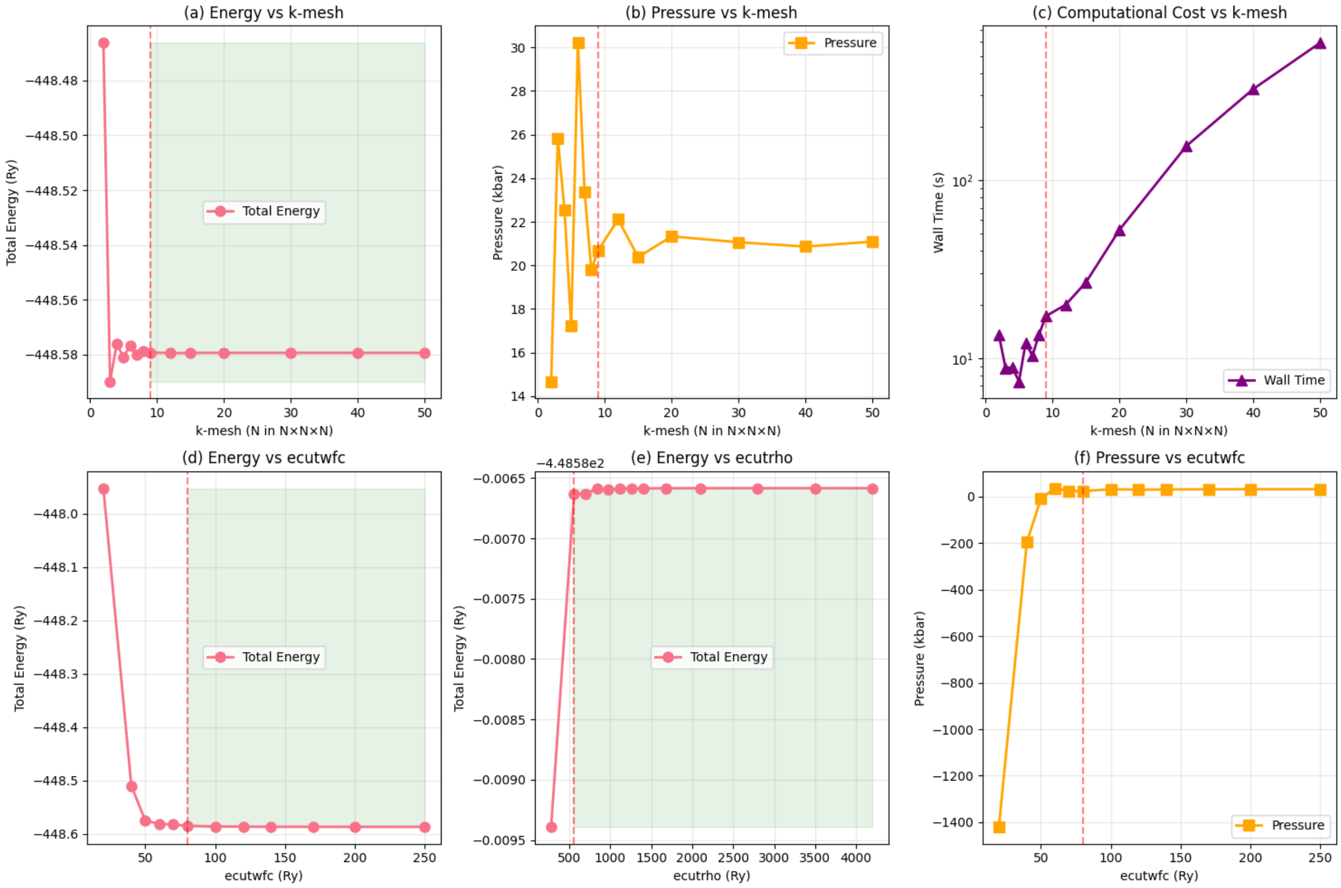

FIG. 5: Graphical representation of the results of the convergence tests.

Appendix B: Characterization of the Ti-Fe, Hf-Fe and Ti-Ni crystals

The third-order Birch–Murnaghan equation of state used for the $E(V)$ plot:

$$E(V) = E_0 + \frac{9V_0B_0}{16}\left\{ \left[\left(\frac{V_0}{V}\right)^{2/3} - 1\right]^3 B_0' + \left[\left(\frac{V_0}{V}\right)^{2/3} - 1\right]^2 \left[6 - 4\left(\frac{V_0}{V}\right)^{2/3}\right] \right\} \tag{B1}$$

Appendix C: Formation energy for Ti-Fe, Hf-Fe and Ti-Ni crystals

TABLE II: Raw calculated results of the final relaxed cells after performing a full 'VC-relax' relaxation. These results were used for the formation-energy calculations. 'TM' is short for 'Total Magnetization'.

Compound	Space group	Tot. energy (Ry/cell)	Vol. (a.u.^{3})	TM (Bohr mag/cell)
TiFe	Pm-3m	−448.58705135	174.11404	0.00
$TiFe_2$ (hex.)	$P6_3$/mmc	−3111.44310946	1035.4493	11.32
$TiFe_2$ (cub.)	Fd-3m	−6222.90178456	2083.0486	22.31
HfFe	Pm-3m	−442.15147748	209.0910	−0.00
$HfFe_2$ (hex.)	$P6_3$/mmc	−3085.80224767	1152.5941	12.35
$HfFe_2$ (cub.)	Fd-3m	−6171.63208584	2312.4261	26.33
TiNi	Pm-3m	−462.58331256	184.3975	0.00
$TiNi_2$ (hex.)	$P6_3$/mmc	−3223.55664273	1019.5414	−0.00
$TiNi_2$ (cub.)	Fd-3m	−6447.12798017	2039.9432	−0.00
Ti (elemental)	(hcp)	−357.75479741	347.0343	0.00
Fe (elemental)	(bcc)	−658.54474437	153.4758	4.33
Hf (elemental)	(hcp)	−225.66097144	304.3438	−0.00
Ni (elemental)	(fcc)	−1373.12396031	293.9144	2.64

TABLE III: Formation energies for the Ti–Fe phases.

Compound	ΔE_f (Ry / fu)	ΔE_f (eV / fu)	ΔE_f (eV / atom)	Comment
TiFe (Pm-3m)	−0.06308003	−0.85824746	−0.42912373	1 Ti + 1 Fe per fu
$TiFe_2$ (hex., $P6_3$/mmc)	−0.06443386	−0.87666725	−0.29222242	1 Ti + 2 Fe per fu
$TiFe_2$ (cubic, $Fd\bar{3}m$)	−0.06637956	−0.90313991	−0.30104664	1 Ti + 2 Fe per fu

TABLE IV: Formation energies for the Hf–Fe phases.

Compound	ΔE_f (Ry / fu)	ΔE_f (eV / fu)	ΔE_f (eV / atom)	Comment
HfFe (Pm-3m)	−0.048619575	−0.66150298	−0.33075149	1 Hf + 1 Fe per fu
$HfFe_2$ (hex., $P6_3$/mmc)	−0.0753318275	−1.02494167	−0.34164722	1 Hf + 2 Fe per fu
$HfFe_2$ (cub., $Fd\bar{3}m$)	−0.0787806400	−1.07186515	−0.35728838	1 Hf + 2 Fe per fu

TABLE V: Formation energies for the Ti–Ni phases.

Compound	ΔE_f (Ry / fu)	ΔE_f (eV / fu)	ΔE_f (eV / atom)	Comment
TiNi (Pm-3m)	−0.05072335	−0.69012624	−0.34506312	1 Ti + 1 Ni per fu
$TiNi_2$ (hex., $P6_3$/mmc)	−0.07558139	−1.02833715	−0.34277905	1 Ti + 2 Ni per fu
$TiNi_2$ (cub., $Fd\bar{3}m$)	−0.07741823	−1.05332861	−0.35110954	1 Ti + 2 Ni per fu

Appendix D: Optimal Hydrogen storage positions at high symmetry sites in TiFe, HfFe and TiNi crystals

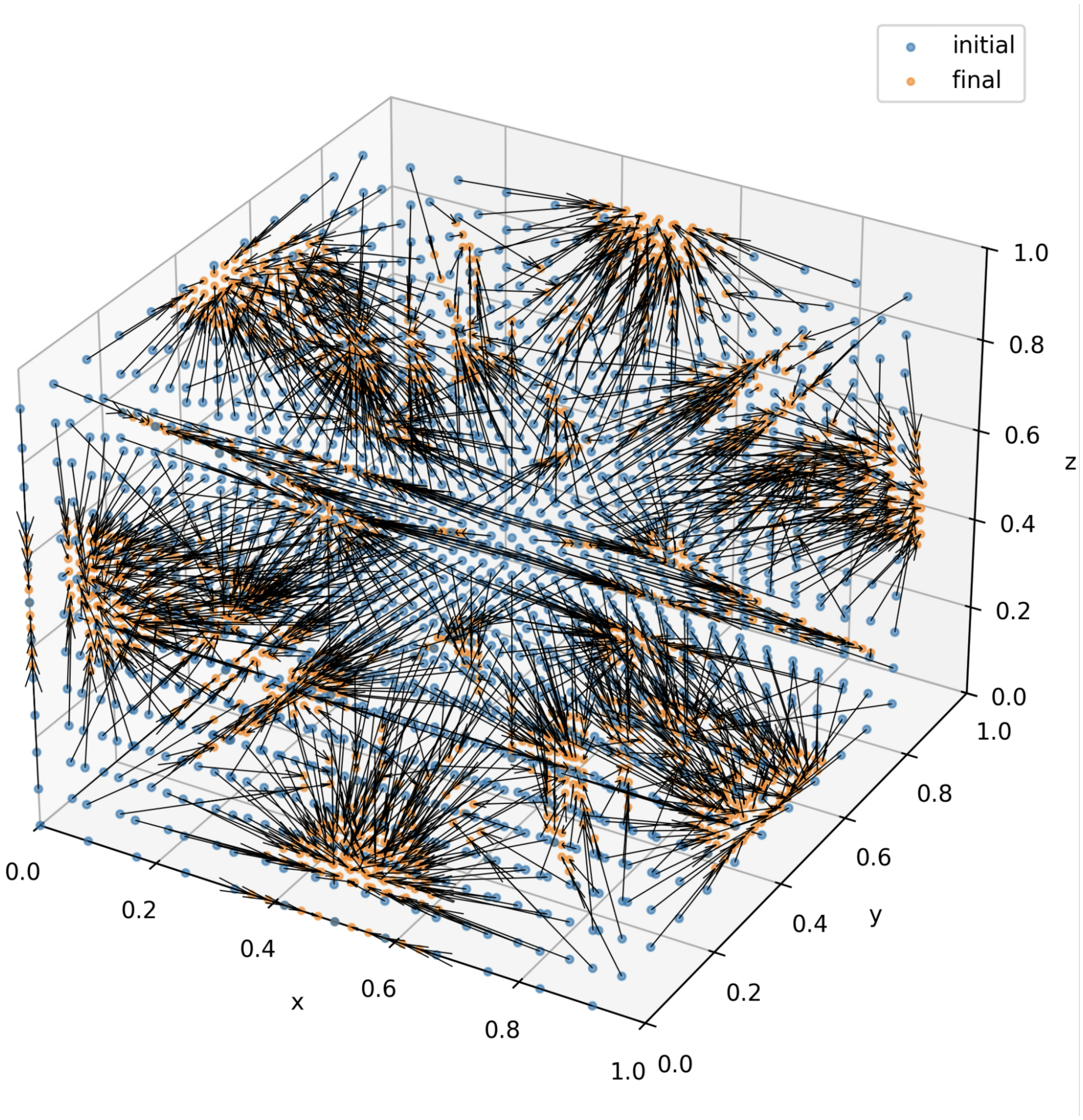

FIG. 6: Graphical representation of the displacement of hydrogen atoms in the TiFe unit cell during DFT relaxation. Arrows indicate the direction of atomic movements toward preferred high-symmetry Wyckoff positions (3c and 3d).

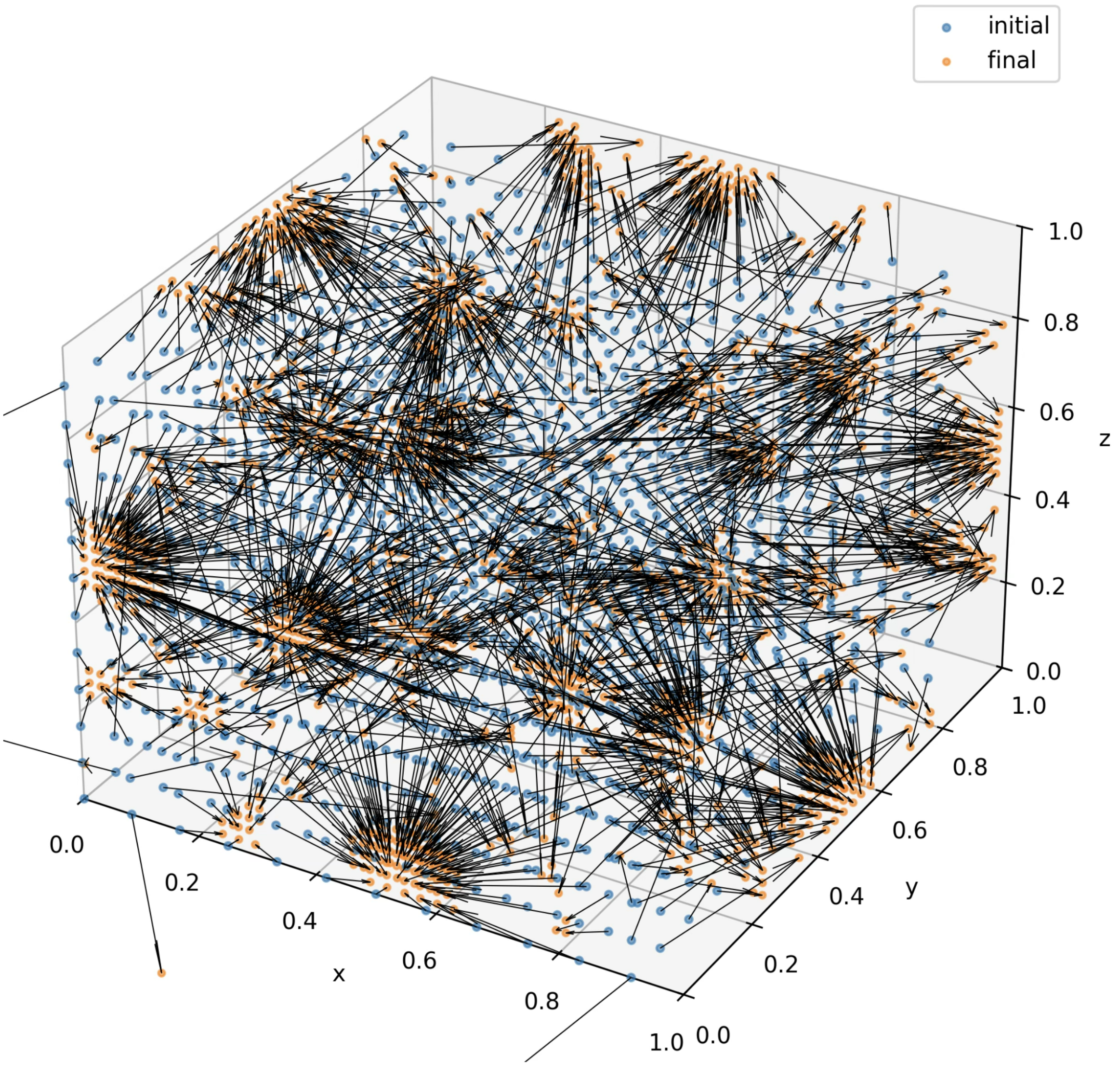

FIG. 7: Graphical representation of the displacement of hydrogen atoms in the HfFe unit cell during DFT relaxation. Arrows indicate the direction of atomic movements toward preferred high-symmetry Wyckoff positions (3c, 3d and 6e).

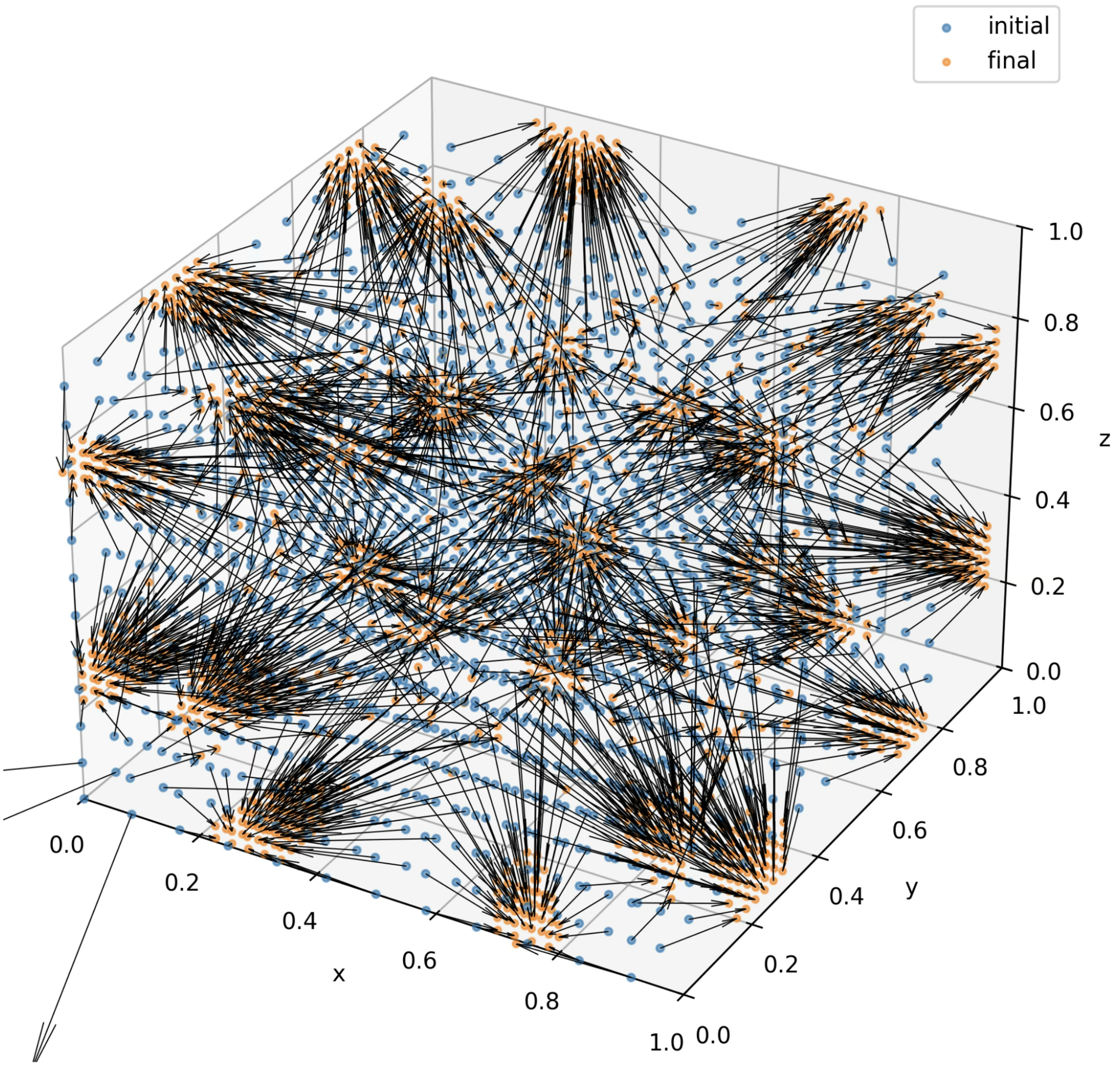

FIG. 8: Graphical representation of the displacement of hydrogen atoms in the TiNi unit cell during DFT relaxation. Arrows indicate the direction of atomic movements toward preferred high-symmetry Wyckoff positions (3c and 6e).

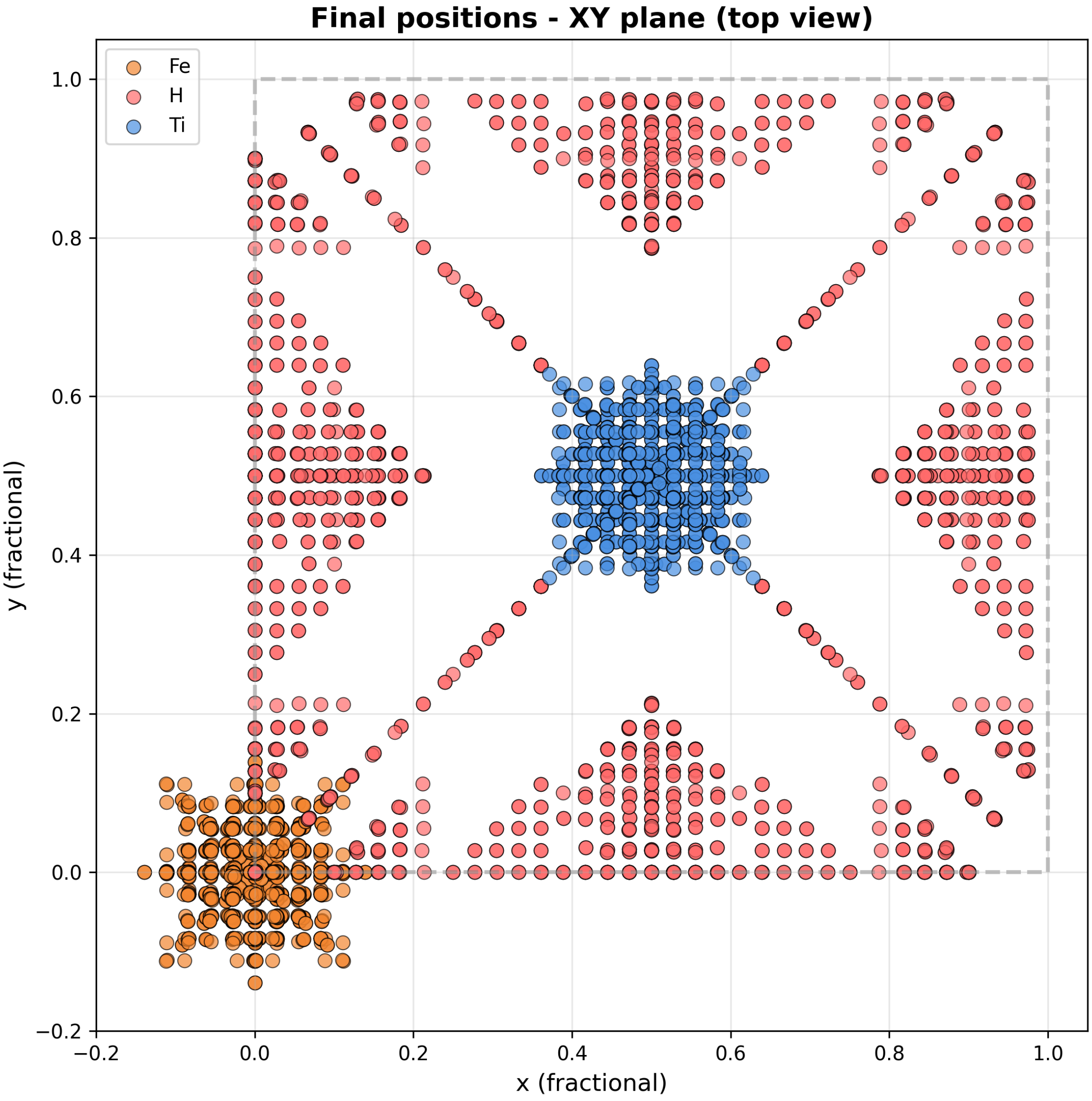

(a) Projection of the final positions of the Fe, H and Ti atoms on the XY (top) plane.

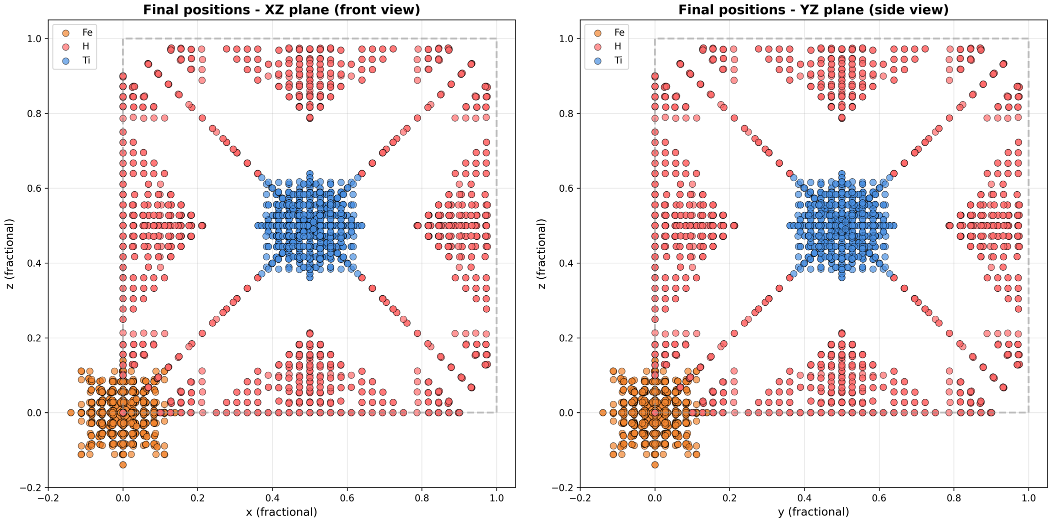

(b) Projection of the final positions of the Fe, H and Ti atoms on the XZ (front) plane.

(c) Projection of the final positions of the Fe, H and Ti atoms on the YZ (side) plane.

FIG. 9: TiFe: projections on the XY (a), XZ (b) and YZ (c) plane of the final positions of the Fe, H and Ti atoms after a ‘relax’ calculation of 1728 separate calculations where one H was placed in a different spot in the unit cell. This plot clarifies the 3D image in Figure 2.

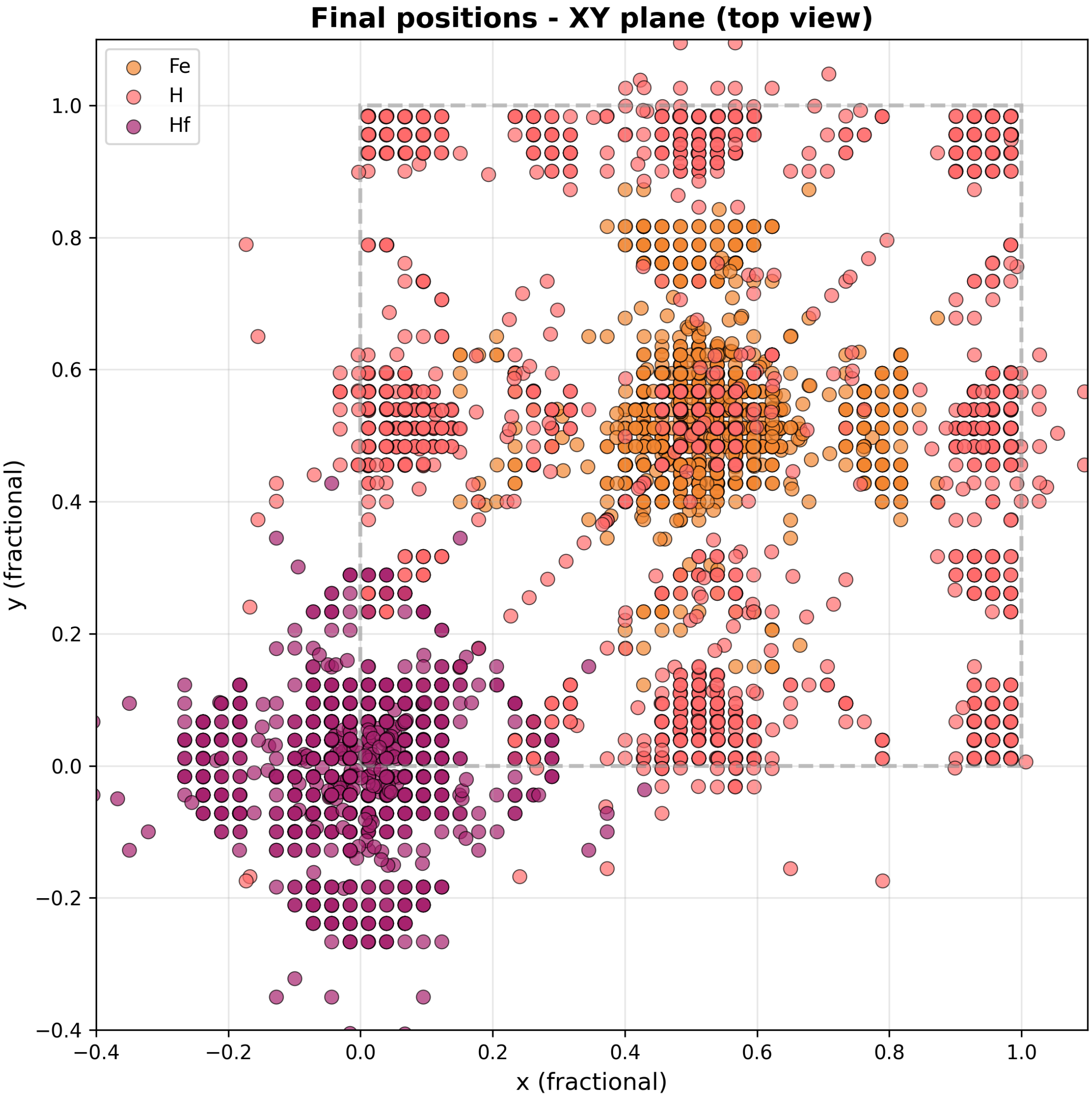
Final positions - XY plane (top view)

(a) Projection of the final positions of the Fe, H and Hf atoms on the XY (top) plane.

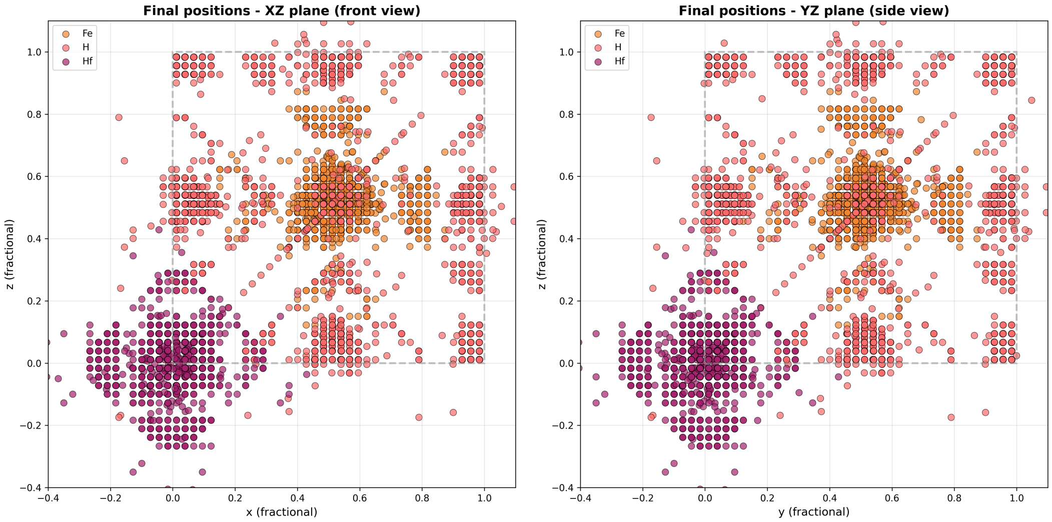
Final positions - XZ plane (front view)

Final positions - YZ plane (side view)

(b) Projection of the final positions of the Fe, H and Hf atoms on the XZ (front) plane.

(c) Projection of the final positions of the Fe, H and Hf atoms on the YZ (side) plane.

FIG. 10: HfFe: projections on the XY (a), XZ (b) and YZ (c) plane of the final positions of the Fe, H and Hf atoms after a ‘relax’ calculation of 1728 separate calculations where one H was placed in a different spot in the unit cell. This plot clarifies the 3D image in Figure 7.

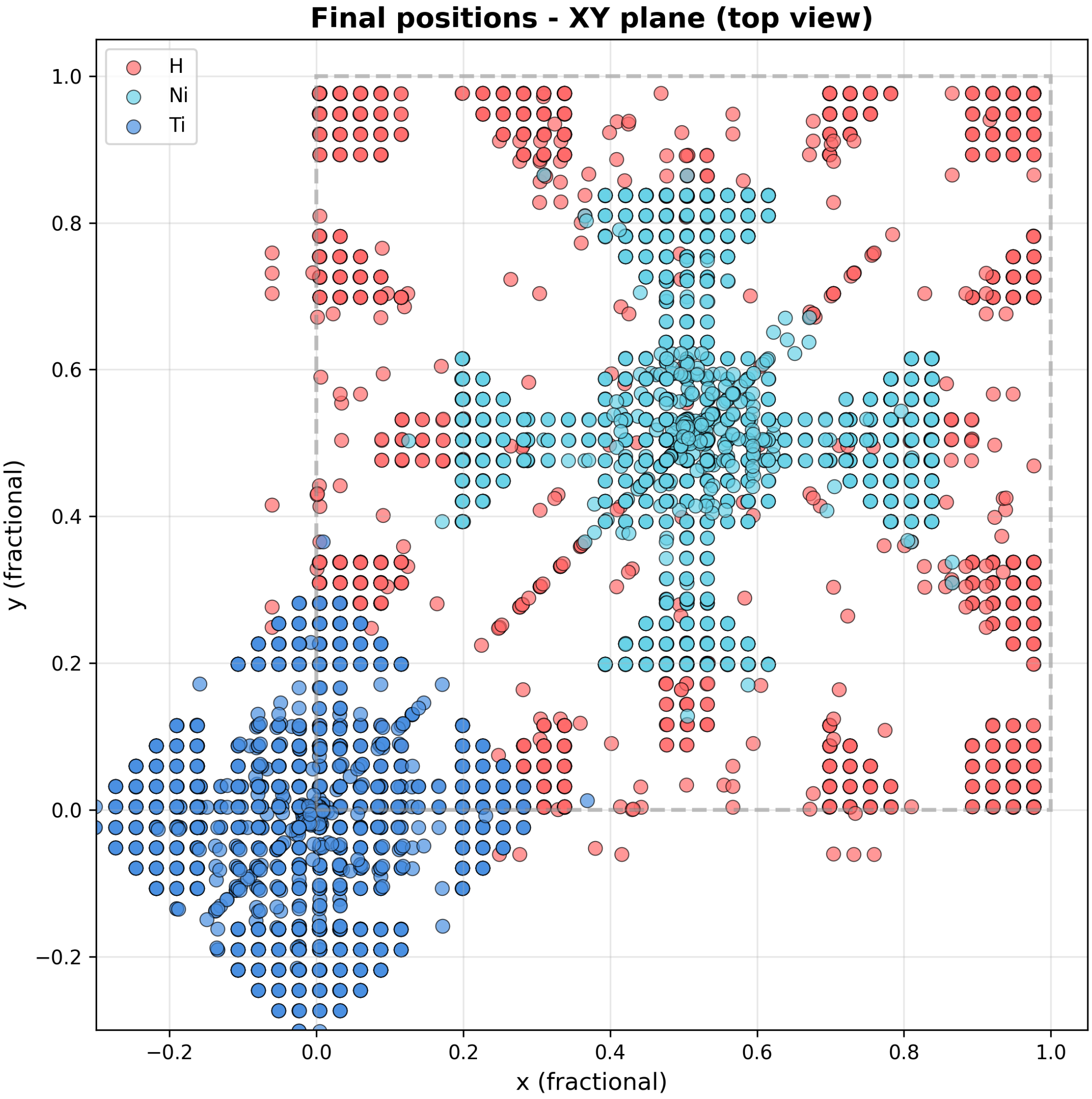

(a) Projection of the final positions of the H, Ni and Ti atoms on the XY (top) plane.

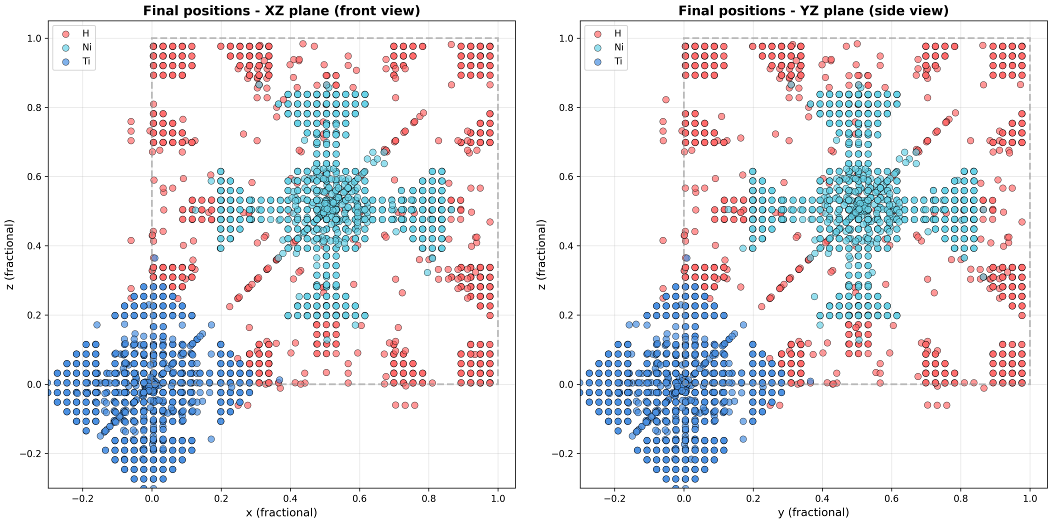

(b) Projection of the final positions of the H, Ni and Ti atoms on the XZ (front) plane.

(c) Projection of the final positions of the H, Ti and Ni atoms on the YZ (side) plane.

FIG. 11: TiNi: projections on the XY (a), XZ (b) and YZ (c) plane of the final positions of the H, Ti and Ni atoms after a ‘relax’ calculation of 1728 separate calculations where one H was placed in a different spot in the unit cell. This plot clarifies the 3D image in Figure 8.

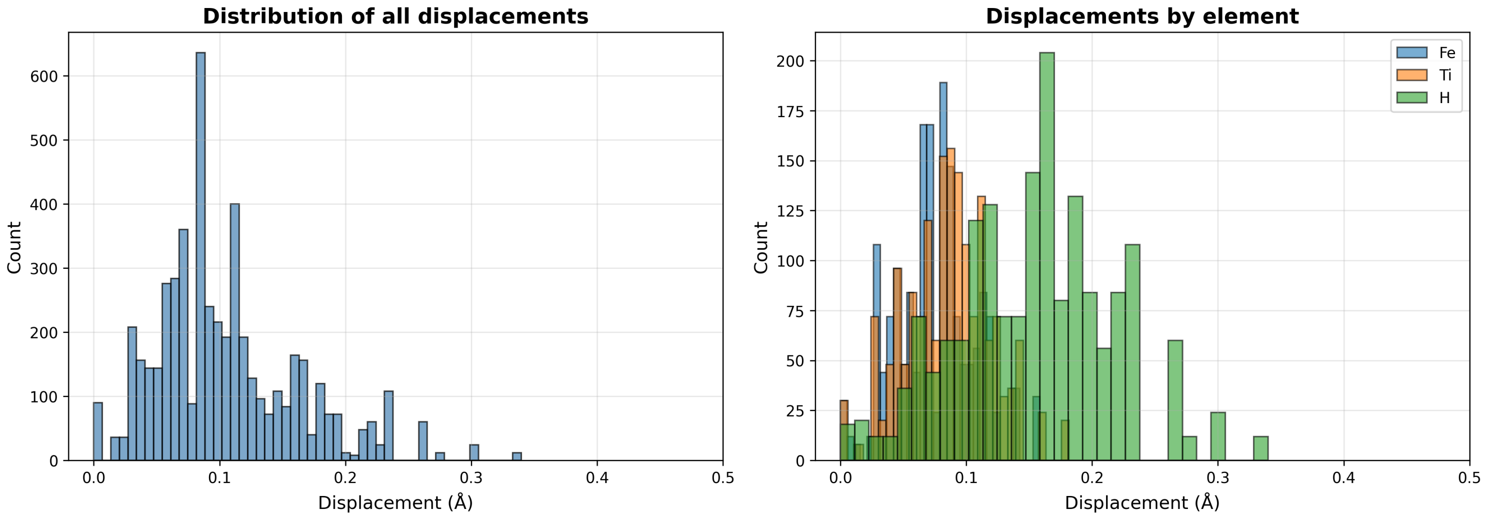

(a) TiFe: displacement histograms of all elements (left) and of the three separate elements (right).

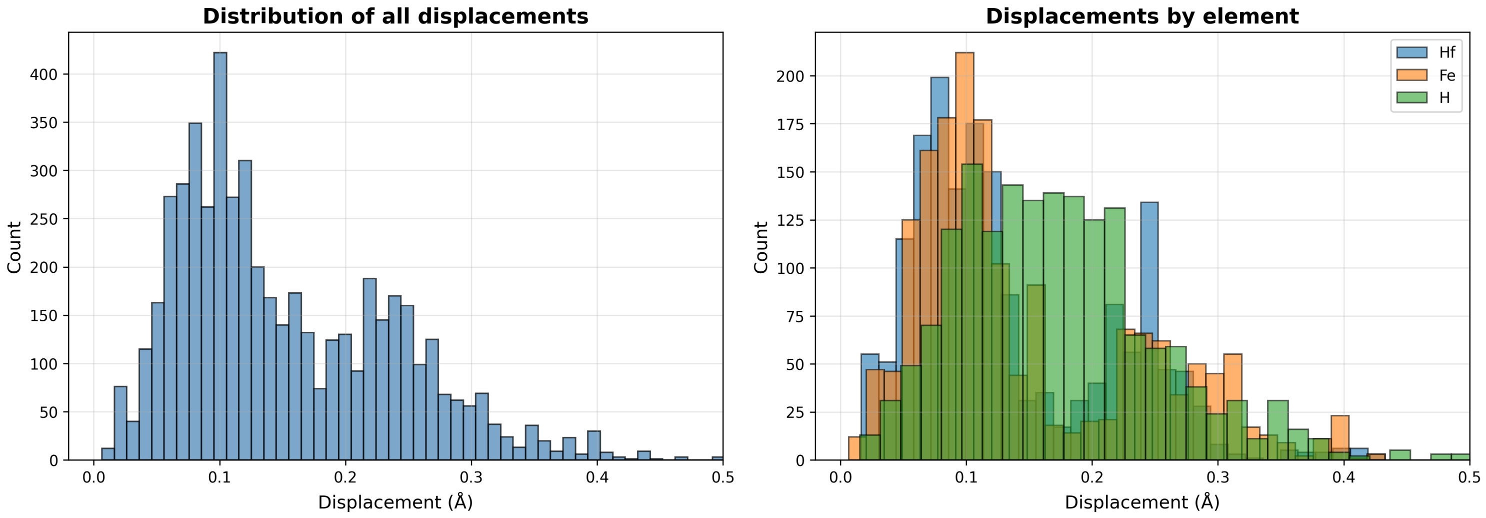

(b) HfFe: displacement histograms of all elements (left) and of the three separate elements (right).

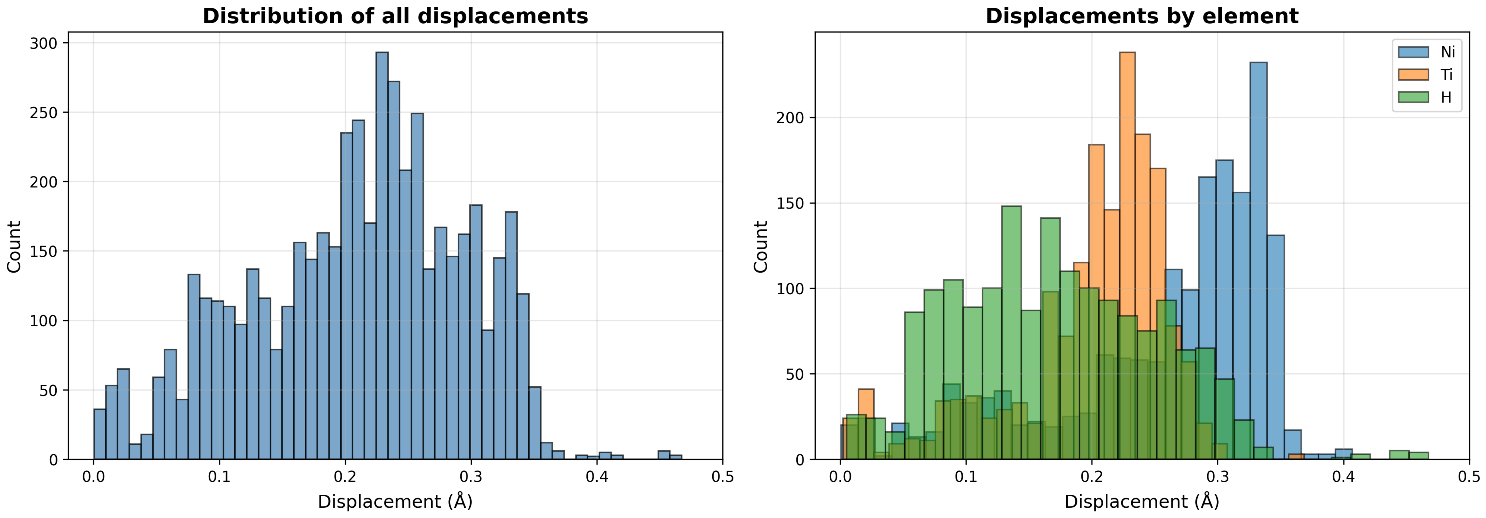

(c) TiNi: displacement histograms of all elements (left) and of the three separate elements (right).

FIG. 12: Displacement histograms of the 1728 seperate runs of the three different crystals [TiFe (a), HfFe (b) and TiNi (c)] showing that the amount of movement is different in the different crystal structures. Also the mobility of the heavier elements lies notably higher in TiNi, compared to the other crystals.

TABLE VI: Summary of *vc-relax* calculations for different hydrogen configurations in HfFe, TiFe, and TiNi: converged energies, volumes, and hydrogen positions, with non-converged cells listed below.

Cell	Label	NH	Energy (Ry)	Volume (a.u.^{3})	E per H (Ry)	Final H positions
HfFe	HfFe_0	0	-442.151477	209.09100	/	/
HfFe	HfFe_1	1	-442.386869	1411.01630	-0.235392	(0.36,0.00,0.00)
HfFe	HfFe_2	1	-442.577943	1000.95584	-0.426465	(0.53,0.00,0.00)
HfFe	HfFe_3	2	-443.533753	1411.01630	-0.691138	(0.36,0.00,0.00), (0.71,0.00,0.00)
HfFe	HfFe_4	2	-443.618928	1411.01630	-0.733725	(0.36,0.00,0.00), (0.53,0.00,0.00)
HfFe	HfFe_5	2	-443.720292	1411.01630	-0.784407	(0.36,0.00,0.00), (0.00,0.36,0.00)
HfFe	HfFe_6	2	-443.446887	1411.01630	-0.647705	(0.00,0.53,0.53), (0.53,0.53,0.00)
HfFe	HfFe_7	2	-443.348912	1411.01630	-0.598717	(0.00,0.53,0.53), (0.53,0.53,0.00)
HfFe	HfFe_8	3	-445.098972	1411.01630	-0.982498	(0.36,0.00,0.00), (0.00,0.36,0.00), (0.00,0.00,0.36)
HfFe	HfFe_9	3	-444.611574	1411.01630	-0.820032	(0.53,0.00,0.00), (0.00,0.53,0.00), (0.00,0.00,0.53)
TiFe	TiFe_0	0	-448.587058	174.09620	/	/
TiFe	TiFe_1	1	-449.753279	191.46800	-1.166221	(0.50,0.50,0.00)
TiFe	TiFe_2	1	-449.678599	197.59560	-1.091541	(0.25,0.25,0.25)
TiFe	TiFe_3	2	-450.922773	207.87020	-1.167857	(0.50,0.50,0.00), (0.00,0.50,0.50)
TiFe	TiFe_4	3	-451.875249	260.71460	-1.096064	(0.50,0.00,0.00), (0.00,0.50,0.00), (0.00,0.00,0.50)
TiFe	TiFe_5	3	-452.076297	230.52230	-1.163080	(0.50,0.50,0.00), (0.00,0.50,0.50), (0.50,0.00,0.50)
TiNi	TiNi_0	0	-462.583313	184.39750	/	/
TiNi	TiNi_1	2	-464.159552	1244.37620	-0.788120	(0.34,0.00,0.00), (0.68,0.00,0.00)
TiNi	TiNi_2	2	-464.217511	1244.37620	-0.817099	(0.34,0.00,0.00), (0.00,0.68,0.00)
TiNi	TiNi_3	2	-464.213042	1244.37620	-0.814865	(0.34,0.00,0.00), (0.00,0.34,0.00)
TiNi	TiNi_4	3	-465.372369	1244.37620	-0.929685	(0.34,0.00,0.00), (0.00,0.34,0.00), (0.00,0.00,0.34)
TiNi	TiNi_5	3	-465.377947	1244.37620	-0.931545	(0.68,0.00,0.00), (0.00,0.34,0.00), (0.00,0.00,0.34)

Non-converged cells:

Cell	NH	Initial H positions
HfFe	1	(0.50,0.50,0.00)
HfFe	2	(0.33,0.00,0.00), (0.00,0.33,0.00)
HfFe	2	(0.33,0.00,0.00), (0.00,0.66,0.00)
TiNi	1	(0.33,0.00,0.00)
TiNi	1	(0.50,0.50,0.00)
TiNi	2	(0.50,0.50,0.00), (0.50,0.00,0.50)
TiNi	3	(0.50,0.50,0.00), (0.50,0.00,0.50), (0.00,0.50,0.50)
TiNi	3	(0.33,0.00,0.00), (0.00,0.33,0.00), (0.00,0.00,0.66)